

1
2
3
4
5
6
7
8
9
10
11
12
13
14
15
16
17
18
19
20
21
22
23
24
25
26

**Theoretical analysis of mixing in liquid clouds. Part IV: DSD evolution
and mixing diagrams**

Mark Pinsky, and Alexander Khain

Department of Atmospheric Sciences, The Hebrew University of Jerusalem, Israel

Submitted to

Atmospheric Chemistry and Physics

May 2017

Revised September 2017

Second revision: November 2017

Communicating author: Alexander Khain, The Hebrew University of Jerusalem,
khain@vms.huji.ac.il

27

28 **Abstract**

29 Evolution of droplet size distribution (DSD) due to mixing between cloudy and dry
30 volumes is investigated for different values of the cloud fraction and for different initial DSD
31 shapes. The analysis is performed using a diffusion-evaporation model which describes time-
32 dependent processes of turbulent diffusion and droplet evaporation within a mixing volume.
33 Time evolution of the DSD characteristics such as droplet concentration, LWC and mean
34 volume radii is analyzed. The mixing diagrams are plotted for the final mixing stages. It is
35 shown that the difference between the mixing diagrams for homogeneous and inhomogeneous
36 mixing is insignificant and decreases with an increase in the DSD width. The dependencies of
37 normalized cube of the mean volume radius on the cloud fraction were compared with those
38 on normalized droplet concentration and found to be quite different. In case the normalized
39 droplet concentration is used, mixing diagrams do not show any significant dependence on
40 relative humidity in the dry volume.

41 The main conclusion of the study is that traditional mixing diagrams cannot serve as a
42 reliable tool for analysis of mixing type.

43

44 **Keywords:** turbulent mixing, droplet evaporation, DSD evolution, mixing diagram

45

46 **1. Introduction**

47 The effects of mixing of cloudy air with surrounding dry air on cloud microphysics are still
48 the focus of many studies (see overview by Devenish et al., 2012). Processes of mixing are
49 investigated in observations (Yum et al., 2015; Bera et al., 2016a,b), Large Eddy Simulations
50 (Andrejczuk et al., 2009; Khain et al., 2017) and Direct Numerical Simulations (Kumar et al.,
51 2014, 2017). Processes of mixing and their effects on droplet size distributions were recently
52 investigated in a set of theoretical studies (Yang et al., 2016; Korolev et al., 2016 (hereafter,
53 Pt1); Pinsky et al., 2016 a,b).

54 The Pt1 presented analysis of conventional (classical) concept of mixing and introduced the
55 main parameters characterizing homogeneous and extremely inhomogeneous mixing. In the
56 classical concept two volumes, cloudy and droplet free one, mix within an unmovable adiabatic
57 mixing volume. At a monodisperse initial droplet size distribution (DSD), homogeneous mixing
58 leads to a decrease in droplet size and droplet mass content, while the number of droplets
59 remains unchanged. Extremely inhomogeneous mixing is characterized by decreasing the
60 number of droplets due to full evaporation of some fraction of droplets penetrating the initially
61 dry air volume while the DSD shape in the cloud volume remains unchanged. As a result of
62 extremely inhomogeneous mixing, droplet number decreases while the mean volume radii
63 remain unchanged. At a polydisperse DSDs, the extreme homogeneous mixing is characterized
64 by proportional changes in DSD for all droplet radii (Pt1). Since widely used mixing diagrams
65 describe the final equilibrium stage of mixing within the mixing volume they do not contain
66 information about changes in microphysical quantities in the course of mixing.

67 Pinsky et al. (2016a, hereafter Pt2) analyzed the time evolution of initially monodisperse
68 and polydisperse DSD during homogeneous mixing. It was shown that result of mixing
69 strongly depends on the shape of the initial DSD. At a wide DSD, evaporation of droplets
70 (first of all, of the smallest ones) is not accompanied by a decrease in the mean volume or
71 effective radius. Moreover, the values of the radii may even increase over time. This result

72 indicates that the widely used criterion of separation of mixing types based on the behavior of
73 the mean volume radius during mixing is not generally relevant and may be wrong in
74 application to real clouds.

75 Pinsky et.al. (2016b, hereafter Pt3) introduced a diffusion-evaporation model which
76 describes evolution DSDs and all the microphysical variables due to two simultaneously
77 occurring processes: turbulent diffusion and droplet evaporation. Mixing between two equal
78 volumes of subsaturated and cloudy air was analyzed, i.e. it was assumed that the cloud
79 volume fraction $\mu = 1/2$. The initial DSD in the cloudy volume was assumed monodisperse.
80 These simplified assumptions allowed to reduce the turbulent mixing equations to two-
81 parametric ones. The first parameter is the Damköhler number, Da , which is the ratio of the
82 characteristic mixing time to the characteristic phase relaxation time. The second parameter is
83 the potential evaporation parameter R characterizing the ratio between the amount of water
84 vapor needed to saturate the initially dry volume and the amount of available liquid water in
85 the cloudy volume.

86 Within the $Da - R$ space, in addition to the two extreme mixing types defined in the
87 classical concept, two more mixing regimes were distinguished, namely, intermediate and
88 inhomogeneous mixing. It was shown that any type of mixing leads to formation of a tail of
89 small droplets, i.e. to DSD broadening. It was also shown that the relative humidity in the
90 initially dry volume rapidly increases due to both water vapor diffusion and evaporation of
91 penetrating droplets. As a result, the mean volume and effective radii in the initially dry
92 volume rapidly approach the values typical of cloudy volume. At the same time, the liquid
93 water content (LWC) remains significantly lower than that in the cloudy volume during much
94 longer time than required for the effective droplet radius to grow.

95 In the present study (Pt4) we continue investigating the turbulent mixing between an
96 initially droplet free volume (referred to as dry volume) and a cloudy volume. The focus of
97 the study is investigation of DSD temporal evolution and analysis of the final equilibrium

98 DSD. In comparison to Pt3, the problem analyzed in this study is more sophisticated in
99 several aspects:

100 • The dependences of different mixing characteristics on cloud volume fraction $0 \leq \mu \leq 1$
101 are analyzed. In this case the equations of turbulent mixing cannot be reduced to the two-
102 parametric problem as it was done in Pt3.

103 • The initial DSDs in cloud volume are polydisperse. We use both narrow and wide
104 initial DSD described by Gamma distributions with different sets of parameters. The DSD are
105 the same as those used in Pt2. Mechanisms of formation of wide DSDs in clouds including
106 DSDs in undiluted cloud cores were investigated in several studies [e.g., Khain et al., 2000;
107 Pinky and Khain, 2002; Segal et al., 2004; Prabha et al., 2011]. These studies show the DSD
108 broadening is caused by in-cloud nucleation of droplets within clouds as well as by collisions
109 between cloud droplets. It was shown that DSDs in adiabatic volumes can be wide and first
110 raindrops or drizzle drop arise namely in non-diluted adiabatic cloud parcels [Khain et al.,
111 2013; Magaritz-Ronen et al., 2016]. We use both narrow and wide DSDs in the form of
112 Gamma distribution with typical parameters used in different cloud resolving models. The
113 DSDs that are used as initial ones in cloudy volumes could be formed also under influence of
114 mixing during their previous history. The mechanisms of the formation of initial DSD are not
115 of interest in the study since that do not affect the analysis.

116 • The equation for supersaturation, used in this study, is valid at low humidity in the
117 initially dry volume and is more general and compared with that used in Pt3, which makes the
118 DSD calculations more accurate.

119 At the same time, some simplifications used in Pt3 are retained in this study. The vertical
120 movement of the entire mixing volume is neglected; collisions between droplets and droplet
121 sedimentation are not allowed. Also, we consider a 1D diffusion-evaporation problem. We
122 neglect the changes of temperature in the course of mixing, which is possibly a less significant

123 simplification. All these simplifications allow to reveal the effects of turbulent mixing and
 124 evaporation on DSD evolution.

125

126 **2. Formulation of the problem and model design**

127 In this study, the process of mixing is investigated basing on the solution of 1D diffusion-
 128 evaporation equation (see also Pt3). According to this equation, evaporation of droplets due to
 129 negative supersaturation in the mixing volume takes place simultaneously with turbulent
 130 mixing. Since droplets within the volume are under different negative supersaturation values
 131 until the final equilibrium is reached, the modeled mixing is inhomogeneous. The droplets can
 132 evaporate either partially or totally. The evaporation leads to a decrease in droplet sizes and in
 133 droplet concentration.

134 Like in Pt3, the process of turbulent diffusion is described by a 1D equation of turbulent
 135 diffusion. The equation does not describe formation of separate turbulent filaments. Instead, it
 136 describes averaged effects of turbulent vortices of different scales by modeling of turbulent
 137 diffusion, characterized by a typical value of turbulent diffusion coefficient K . The mixing is
 138 assumed to be driven by isotropic turbulence at scales within the inertial sub-range where
 139 Richardson's law is valid. In this case, turbulent coefficient is evaluated as in Monin and
 140 Yaglom (1975):

$$141 \quad K(L) = C\varepsilon^{1/3}L^{4/3} \quad (1)$$

142 In Eq. (1) ε is the turbulent kinetic energy dissipation rate and $C = 0.2$ is a constant (Monin
 143 and Yaglom, 1975), Boffetta and Sokolov (2002). Eq. (1) means that we consider the effects
 144 of turbulent diffusion at scales much larger than the Kolmogorov microscale, i.e. the effects of
 145 molecular diffusion are neglected. In the simulations, we use $L = 40 \text{ m}$ and $\varepsilon = 20 \text{ cm}^2 \text{ s}^{-3}$. It
 146 means that in the present study mixing is performed by vortices smaller than several tens of
 147 meters which agrees with measurements in warm Cu (Gerber et al. 2008). The value of
 148 turbulent kinetic energy dissipation rate chosen is also typical for small Cu (e.g. Gerber et al.

149 2008). These parameters correspond to the values of Da of several hundred. The model allows
 150 utilization of other values of L and ε typical of other cloud type (say, deep convective
 151 clouds) which can change results quantitatively, but not qualitatively.

152

153 *Geometry of mixing and the initial conditions*

154 The conceptual scheme presenting mixing geometry and the initial conditions used in the
 155 following analysis are shown in **Figure 1**.

156

157 **Fig 1 here**

158

159 At $t=0$ the mixing volume of length L is divided into two volumes: the cloud volume of
 160 length μL (Fig.1, left) and the dry volume of length $(1-\mu)L$ (Fig.1, right), where $0 \leq \mu \leq 1$
 161 is the cloud volume fraction. The entire volume is assumed closed, i.e. adiabatic. At $t=0$ the
 162 cloud volume is assumed saturated, so the supersaturation $S_1=0$. This volume is also
 163 characterized by the initial distribution of the square of the droplet radii $g_1(\sigma)$, where $\sigma = r^2$.

164 The initial liquid water mixing ratio in the cloudy volume is equal to

165 $q_{w1} = \frac{4\pi\rho_w}{3\rho_a} \int_0^\infty \sigma^{3/2} g_1(\sigma) d\sigma$. The integral of $g_1(\sigma)$ over σ is equal to the initial droplet

166 concentration in the cloud volume $N_1 = \int_0^\infty g_1(\sigma) d\sigma$. The initial droplet concentration in the

167 dry volume is $N_2=0$, the initial negative supersaturation in this volume is $S_2 < 0$ and the

168 initial liquid water mixing ratio $q_{w2}=0$. Therefore, the initial profiles of these quantities

169 along the x -axis are step functions:

170

$$171 \quad N(x,0) = \begin{cases} N_1 & \text{if } 0 \leq x < \mu L \\ 0 & \text{if } \mu L \leq x < L \end{cases} \quad (2a)$$

$$172 \quad S(x, 0) = \begin{cases} 0 & \text{if } 0 \leq x < \mu L \\ S_2 & \text{if } \mu L \leq x < L \end{cases} \quad (2b)$$

$$173 \quad q_w(x, 0) = \begin{cases} q_{w1} & \text{if } 0 \leq x < \mu L \\ 0 & \text{if } \mu L \leq x < L \end{cases} \quad (2c)$$

174

175 The initial profile of droplet concentration is shown in Fig. 1b. This is the simplest
 176 inhomogeneous mixing scheme, wherein mixing takes place only in the x -direction, and the
 177 vertical velocity is neglected.

178 Since the total volume is adiabatic, the fluxes of different quantities through the left and
 179 right boundaries at any time instance are equal to zero, i.e.

180

$$181 \quad \frac{\partial N(0, t)}{\partial x} = \frac{\partial N(L, t)}{\partial x} = 0; \quad \frac{\partial q_w(0, t)}{\partial x} = \frac{\partial q_w(L, t)}{\partial x} = 0; \quad \frac{\partial q_v(0, t)}{\partial x} = \frac{\partial q_v(L, t)}{\partial x} = 0 \quad (3)$$

182 where q_v is the water vapor mixing ratio.

183 To investigate of mixing process for different initial DSD, we assume that DSD in the cloud
 184 volume can be represented by a Gamma distribution:

$$185 \quad f(r, t = 0) = \frac{N_0}{\Gamma(\alpha)\beta} \left(\frac{r}{\beta}\right)^{\alpha-1} \exp\left(-\frac{r}{\beta}\right) \quad (4)$$

186 where N_0 is an intercept parameter, α is a shape parameter and β is a slope parameter of
 187 distribution. The DSD $f(r)$ relates to distribution $g_1(\sigma)$ as $f(r) = 2rg_1(\sigma)$. We performed
 188 simulations with both initially wide and narrow DSDs. The width of DSD is determined by a
 189 set of parameters. The parameters of the initial Gamma distributions used in this study are
 190 presented in **Table 1**. Parameters of the distributions are chosen in such a way that the modal
 191 radii of DSD and the values of LWC are the same for both distributions. These distributions
 192 were used in Pt2 for analysis of homogeneous mixing.

193

194 **Table 1 here**

195

196

197 **Conservative quantity** $\Gamma(x,t)$

198 The supersaturation equation for an adiabatic immovable volume can be written in the

199 form $\frac{1}{S+1} \frac{dS}{dt} = -A_2 \frac{dq_w}{dt}$, where S is supersaturation over water, and the coefficient200 $A_2 = \frac{1}{q_v} + \frac{L_w^2}{c_p R_v T^2}$ is slightly dependent on temperature (Korolev and Mazin, 2003) (notations201 of other variables are presented in **Appendix**). In our analysis we consider A_2 to be a

202 constant. As follows from the supersaturation equation, the quantity

203

204
$$\Gamma(x,t) = \ln[S(x,t)+1] + A_2 q_w(x,t) \quad (5)$$

205

206 is a conservative quantity, i.e. it is invariant with respect to phase transitions. In Eq. (5),

207 $|S(x,t)|$ can be comparable with unity by the order of magnitude. The conservative quantity208 $\Gamma(x,t)$ obeys the following equation for turbulent diffusion

209

210
$$\frac{\partial \Gamma(x,t)}{\partial t} = K \frac{\partial^2 \Gamma(x,t)}{\partial x^2} \quad (6)$$

211

212 with the adiabatic (no flux) condition at the left and right boundaries $\frac{\partial \Gamma(0,t)}{\partial x} = \frac{\partial \Gamma(L,t)}{\partial x} = 0$ 213 and the initial profile at $t = 0$

214

215
$$\Gamma(x,0) = \begin{cases} A_2 q_{w1} & \text{if } 0 \leq x < \mu L \\ \ln[S_2 + 1] & \text{if } \mu L \leq x < L \end{cases} \quad (7)$$

216

217 From Eq. (7) it follows that $\Gamma(x,0)$ is positive in the cloud volume and negative in the
 218 initially dry volume. The mean value of function $\Gamma(x,0)$ can be written as follows:

219

$$220 \quad \bar{\Gamma} = \frac{1}{L} \int_0^L \Gamma(x,0) dx = \frac{A_2 q_{w1}}{L} \int_0^{\mu L} dx + \frac{\ln[S_2 + 1]}{L} \int_{\mu L}^L dx = \mu A_2 q_{w1} + (1 - \mu) \ln[S_2 + 1] \quad (8)$$

221

222 $\bar{\Gamma}$ can be either positive or negative. In the latter case a complete evaporation of droplets in the
 223 course of mixing takes place.

224 The solution of Eq. (6) with the initial condition (7) is (Polyanin et al., 2004):

$$225 \quad \Gamma(x,t) = \sum_{n=0}^{\infty} a_n \exp\left(-\frac{Kn^2 \pi^2 t}{L^2}\right) \cos\left(\frac{n\pi x}{L}\right) =$$

$$\mu A_2 q_{w1} + (1 - \mu) \ln[S_2 + 1] - \quad (9)$$

$$2 \left(\ln[S_2 + 1] - A_2 q_{w1} \right) \sum_{n=1}^{\infty} \frac{\sin(n\pi\mu)}{n\pi} \exp\left(-\frac{Kn^2 \pi^2 t}{L^2}\right) \cos\left(\frac{n\pi x}{L}\right)$$

226 One can see that function $\Gamma(x,t)$ depends on three independent parameters $A_2 q_{w1}$, S_2 and μ .

227 This function does not depend on the shape of the initial DSD in the cloud volume. In the final
 228 state when $t \rightarrow \infty$, $\Gamma(x,t)$ is :

$$229 \quad \Gamma(t = \infty) = \mu A_2 q_{w1} + (1 - \mu) \ln[S_2 + 1] \quad (10)$$

230 Therefore, $\Gamma(t = \infty)$ depends on the cloud fraction and the initial values of liquid water
 231 mixing ratio in the cloud volume and the relative humidity in initially dry volume.

232 The final equilibrium values of supersaturation $S(x,\infty)$ and liquid water mixing ratio

233 $q_w(x,\infty)$ can be calculated using Eq. (5). The case $\Gamma(t = \infty) > 0$ corresponds to the

234 equilibrium state with $S(x,\infty) = 0$ and $q_w(x,\infty) = \mu q_{w1} + (1 - \mu) \frac{\ln[S_2 + 1]}{A_2}$, when droplets

235 remain, but do not evaporate any longer.

236 The case $\Gamma(t=\infty) < 0$ corresponds to the equilibrium state with $q_w(x, \infty) = 0$ and
 237 $S(x, \infty) = (1 + S_2)^{1-\mu} \exp(\mu A_2 q_{w1}) - 1$. In this equilibrium state droplets are totally evaporated,
 238 and volume remains subsaturated $S(x, \infty) < 0$. At given q_{w1} and S_2 , there is a critical value of
 239 the cloud fraction μ_{cr} which separates these two possible final equilibrium states. This critical
 240 value corresponds to $\Gamma(t = \infty) = 0$ and can be calculated from Eq. (10) as:

241

$$242 \quad \mu_{cr} = \frac{\ln[S_2 + 1]}{\ln[S_2 + 1] - A_2 q_{w1}} \quad (11)$$

243

244 Another expression for μ_{cr} was formulated in Pt1.

245 The examples of spatial-temporal variations of function $\Gamma(x, t)$ for different cloud
 246 fractions and initial RH=80% are shown in **Figure 2**.

247

248 **Fig 2 here**

249

250 Upper panels $\mu = 0.1$ correspond to the case of final total droplet evaporation and negative
 251 final function Γ , whereas the middle and bottom rows $\mu = 0.5$ and $\mu = 0.9$ illustrate partial
 252 evaporation cases when the total mixing volume reaches saturation. It is interesting that the
 253 time required for the final equilibrium state to be reached practically does not depend on the
 254 cloud fraction, being ~ 180 seconds for the illustrated cases. The cases $\mu = 0.1$ and $\mu = 0.9$
 255 demonstrate a strong non-symmetric spatial variability of $\Gamma(x)$ function during the first 50
 256 seconds. At $\mu = 0.5$, a nearly full compensation between saturation deficit in the dry volume
 257 and available liquid water in the cloud volume takes place if at the equilibrium state
 258 $S(x, \infty) = q_w(x, \infty) = \Gamma(x, \infty) = 0$. However, the compensation at $\mu = 0.5$ is not full because of
 259 the nonlinearity of Γ in Eq. (5).

260

261 ***Diffusion-evaporation equation for DSD***

262 To formulate the diffusion-evaporation equation we use a simplified equation for droplet
 263 evaporation (Pruppacher and Klett, 1997), in which the curvature term and the chemical
 264 composition term are omitted

$$265 \quad \frac{d\sigma}{dt} = \frac{2S}{F} \quad (12)$$

266 where $F = \frac{\rho_w L_w^2}{k_a R_v T^2} + \frac{\rho_w R_v T}{e_w(T)D} = \text{const}$ (Notations of other variables are presented in Appendix.)

267 The solution of Eq. (12) is

$$268 \quad \sigma(t) = \frac{2}{F} \int_0^t S(t') dt' + \sigma_0 \quad (13)$$

269 Eq. (13) means that in the course of evaporation, distribution $g(\sigma)$ shifts to the left without
 270 changing its shape. The diffusion-evaporation equation for function $g(x, t, \sigma)$ can be written
 271 in the form

272

$$273 \quad \frac{\partial g}{\partial t} = K \frac{\partial^2 g}{\partial x^2} + \frac{\partial}{\partial \sigma} \left(\frac{d\sigma}{dt} g \right) \quad (14)$$

274 Combining Eqs. (12) and (14) yields

$$275 \quad \frac{\partial g(x, t, \sigma)}{\partial t} = K \frac{\partial^2 g(x, t, \sigma)}{\partial x^2} + \frac{2S}{F} \frac{\partial g(x, t, \sigma)}{\partial \sigma} \quad (15)$$

276

277 Eq. (15) is similar to the diffusion-evaporation equation for size distribution function used in
 278 Pt 3. The first term on the right hand side of Eq. (15) describes the effect of turbulent
 279 diffusion, while the second term describes the changes of size distribution due to droplet
 280 evaporation. To close this equation, one can use Eq. (5) written as

281

282 $S(x,t) = \exp[\Gamma(x,t) - A_2 q_w(x,t)] - 1,$ (16)

283

284 and the equation for liquid water mixing ratio

285

286 $q_w(x,t) = \frac{4\pi\rho_w}{3\rho_a} \int_0^\infty \sigma^{3/2} g(x,t,\sigma) d\sigma$ (17)

287 The equation system (15-17) for distribution $g(x,t,\sigma)$ should be solved under the following

288 initial condition

289 $g(x,0,\sigma) = \begin{cases} g_1(\sigma) & \text{if } 0 \leq x < \mu L \\ 0 & \text{if } \mu L \leq x < L \end{cases}$ (18)

290 and using the Neumann boundary conditions

291

292 $\frac{\partial g(0,t,\sigma)}{\partial x} = \frac{\partial g(L,t,\sigma)}{\partial x} = 0$ (19)

293

294 These equations were solved numerically on a linear grid of droplet radii r_j being within

295 the range 0-50 μm , where $j = 1 \dots 50$ are the bin numbers. The number of grid points along the

296 x -axis was set equal to 81. In numerical calculations, the “evaporation term” in Eq. (15) was

297 approximated as

298 $\frac{2S}{F} \frac{\partial g(x,t,\sigma)}{\partial \sigma} \approx \frac{g\left(x,t,\sigma + \frac{2S}{F} \Delta t\right) - g(x,t,\sigma)}{\Delta t}.$ (20)

299

300 A shift and subsequent remapping of DSD using the method proposed by Kovetz and Olund’s

301 (1969) were implemented to solve Eq. (20) with the help of MATLAB solver PDEPE. After

302 calculation of $g(x,t,\sigma_j)$ function, DSD $f(x,t,r_j)$ was calculated using the relationship

303 $f(x,t,r_j) = 2r_j g(x,t,\sigma_j).$

304

305 **3. Spatial-temporal variations of DSD and of DSD parameters**

306 Mixing may take a significant time. Cloud microphysical parameters measured in *in-situ*
307 observations correspond to different stages of this transient mixing process. During mixing,
308 DSDs and its parameters change substantially, which makes it reasonable to analyze these
309 time changes.

310 **Figure 3** shows time evolution of initially narrow DSD in the centers of the cloudy volume
311 and of the initially dry volume. The values of DSD in the initially cloudy volume decrease
312 while there are no significant changes in the DSD shape. At $\mu=0.7$, the droplet radius
313 corresponding to the DSD maximum remains unchanged during mixing staying equal to 10
314 μm . At $\mu=0.3$ the effect of droplet diffusion on DSD is stronger, and mixing leads not
315 only to a decrease in the DSD values, but also to a decrease in the peak droplet radius in the
316 cloudy volume. Both at $\mu=0.3$ and $\mu=0.7$, mixing leads to broadening of the initial DSD
317 due to the appearance of the tail of small droplets. **The tail of small droplets is especially**
318 **pronounced in the initially dry volume since maximum evaporation of penetrated droplets.**

319 The rate of the DSD growth in the initially dry volume, depends on the value of the cloud
320 fraction. At a low cloud fraction, DSD maximum (**i.e. drop concentration and drop mass**)
321 remains substantially lower for the most period of mixing process than that in the cloudy
322 volume. At the same time, the radius corresponding to the DSD maximum increases reaching
323 80% of its maximum value already within the first 5 s. This is due to the fast increase in the
324 relative humidity during mixing, so large droplets penetrating the initially dry volume do not
325 decrease in size anyhow significantly determining the values of modal, mean volume and
326 effective radii. Thus, we see two stages of DSD evolution within in the initially dry volumes:
327 at the first stage penetrated droplets evaporate totally or partially forming the tail of small
328 droplets. The formation of the tail of smallest droplets does not lead to a significant changes
329 of the size of the largest droplets. Note that according to equation of diffusion

330 growth/evaporation in of sub-saturation conditions, the rate of droplet radii decreases inverse
331 proportionally to the droplet radius. It means that if, say, radius of a 2 μm droplet decreases
332 twice during a certain time instance, the radius of 20 μm droplet will decrease by less than
333 0.1 μm , i.e. remains approximately unchanged. At this stage diffusion of water vapor from
334 cloudy volume and evaporation of penetrating droplets lead to a rapid growth of relative
335 humidity RH. This growth of RH decreases evaporation rate of droplets penetrating initially
336 dry volume later. At the second stage mixing leads to the increase in the droplet number due
337 to droplet diffusion from cloudy volume. Since, RH is high, this diffusion is not accompanied
338 by significant change droplet sizes, so DSD grows similarly at all radii.

339

340 **Figure 3 here**

341

342 At the initially wide DSD (**Figure 4**), the radii of the DSD maximum do not change. It
343 means that at the initial RH= 80%, mixing and evaporation lead to a fast saturation of the
344 initially dry volume, after which the peak radius remains unchanged in this volume. **In the**
345 **initially cloud volume RH remains close to 100% so the DSD decrease is related to dilution by**
346 **the air from initially dry volume.**

347

348 **Figure 4 here**

349

350 It is interesting that at $\mu = 0.3$ in the initially dry volume, DSD reaches its maximum during
351 the transition period (Fig.4, at $t=80\text{s}$), and then decreases toward the equilibrium state. This
352 behavior is caused by the competition between the diffusion and droplet evaporation.

353 **Figure 5** shows spatial dependences of droplet concentration, LWC and the mean volume
354 radius within the mixing volume at different time instances at narrow initial DSD. At small
355 values of the cloud fraction, diffusion of water vapor and droplets, as well as droplet

356 evaporation lead to a fast decrease in droplet concentration and in LWC in the initially cloud
 357 volume. The mean volume radius in this volume decreases by about 15% in the course of
 358 mixing. It is natural that at large cloud fraction, droplet concentration and LWC in the initially
 359 cloudy volume decrease slowly, while these quantities in the initially dry volume increase
 360 rapidly. At both small and large cloud fractions, the mean volume radius in the initially dry
 361 volume grows rapidly during the mixing toward its values in the initially cloudy volumes,
 362 even if droplet concentration and LWC remain much lower than in the adjacent cloud volume.

363

364 **Figure 5 here**

365

366 **Figure 6** shows the spatial dependences of droplet concentration, LWC and the mean
 367 volume radius within the mixing volume at different time instances at wide initial DSD.

368

369

370 **Figure 6 here**

371

372

373 A specific feature of mixing at a wide DSD is the increase in the mean volume radius, so the

374 ratio $\frac{r_v}{r_{v0}} > 1$. In the course of mixing, the mean volume radius maximum is reached in the

375 initially dry volumes. This result can be attributed to the fact that in this volume smaller

376 droplets fully evaporate, so the concentration of large droplets increases with respect to

377 concentration of smaller droplets (Fig. 4, right column). Scattering diagrams plotted using *in-*

378 *situ* observations often contain points or groups of points with $\frac{r_v}{r_{v0}} > 1$ (or $\frac{r_e}{r_{e0}} > 1$, where r_e is

379 effective radius) within wide range of normalized droplet concentration (e.g., Burnet and

380 Brenguier, 2007; Krueger et al., 2006, Gerber et al., 2008). The result obtained in the present

381 study shows that the behavior of $\frac{r_v}{r_{v0}}$ with time in the course of mixing may depend of the
 382 DSD shape in the initially cloud volume that determines relationship between concentrations
 383 of small and large droplets in course of mixing. Of course, the DSD shape is only one possible
 384 reason of appearance of points with $\frac{r_v}{r_{v0}} > 1$ on the scattering diagram.

385 We see that the transition to the final equilibrium state within the volume with the spatial
 386 scale of 40 m is about 5 min (Fig. 8), which is a comparatively long period of time compared
 387 to the characteristic times of other microphysical processes, including droplet evaporation.
 388 During this time the DSD changes substantially, especially at small cloud fraction. The mean
 389 volume radius in the initially dry volume increases much faster than LWC. As a result, mean
 390 volume radius in such volume rapidly reaches the values typical of cloudy air, while LWC
 391 still remains substantially lower than in the cloudy volume. Despite some DSD broadening,
 392 the final DSDs in the mixing volume resemble those in the initially cloud volumes. The main
 393 effect of mixing is lowering the DSD values as the cloud fraction decreases.

394

395 **4. Equilibrium state and mixing diagram**

396 This study reconsiders the classical theory of mixing diagrams. In the classical theory
 397 two volumes (cloudy and droplet free) mix with each other within a given unmovable mixing
 398 volume (see review by Korolev et al., 2016). Mixing diagrams are typically plotted for times
 399 when all variables become uniform within the mixing volume, i.e when the equilibrium state
 400 is reached. We plot the mixing diagram using the same simplifications used in the plotting
 401 classical mixing diagrams, namely: no vertical motions and no collisions are assumed. These
 402 assumptions allow to reveal better the microphysical effects of turbulent mixing. It is widely
 403 assumed that the mixing type is determined by the Damkohler number that depends only on
 404 drop relaxation time and mixing time. No averaged vertical velocity and no collision rate are
 405 included into this criterion.

406 We extend the theory, however, in several important aspects concerning microphysical
 407 effects: a) we consider time dependent process of mixing and b) initial droplet size
 408 distributions are assumed polydisperse.

409 Mixing considered in the present study always leads to the equilibrium state. As was
 410 explained above, two equilibrium states are possible. The first one is characterized by the total
 411 evaporation of cloud droplets $q_w(x, \infty) = 0$, whereas the second one occurs if the air in the
 412 mixing volume becomes saturated, i.e. when $S(x, \infty) = 0$. At the given initial values of q_{w1} in
 413 the cloud volume and of S_2 in the initially dry volume, there always exists the cloud fraction
 414 μ_{cr} (Eq. 11) separating these two states.

415

416 **4.1. The process of achieving the equilibrium state**

417 **Figure 7** shows the dependences of the time required to reach the equilibrium on the cloud
 418 fraction, at different initial relative humidity values in the dry volume and two initial DSDs
 419 (the parameters are presented in Tab.1). The characteristic time is defined here as the time

420 from the beginning of mixing to the time instance when inequality $\delta = \frac{\bar{N}(t) - \bar{N}(\infty)}{\bar{N}(0) - \bar{N}(\infty)} < 0.01$

421 becomes valid. The mean droplet concentration is calculated by averaging along x -axes

422 $(\bar{N}(t) = \frac{1}{L} \int_0^L N(x, t) dx)$. In case of a total evaporation, $\bar{N}(\infty) = 0$.

423

424 **Figure 7 here**

425

426 Each curve in Fig. 7 consists of two branches. The left branches correspond to the total
 427 evaporation regime, while the right branches correspond to the partial evaporation at
 428 equilibrium. The maximum time corresponds to the situation when the available amount of
 429 liquid water is approximately equal to the saturation deficit. A similar result was obtained in

430 Pt1 and Pt2 for homogeneous mixing. The maximum values of the characteristic time are
 431 about 4 min for a mixing volume of 40 m in length. The right branches show that the
 432 characteristic time decreases with increasing cloud fraction. Despite some differences in the
 433 curve slopes, the characteristic times for wide and narrow DSD are quite similar.

434 **Figure 8** shows dependences of normalized cube of the mean volume radius on the cloud
 435 fraction at different time instances for two values of x : $x = 0$ (solid lines) corresponds to the
 436 initially cloudy volume, and $x = L$ (dashed line) corresponds to the initially dry volume. The
 437 figure is plotted for the narrow DSD for two values of RH_2 : 60% and 95%. Despite the fact
 438 that the diffusion-evaporation equation allows simulating using any initial RH, we do not
 439 consider in our examples the cases of very low RH of dry volume. It is because at very low
 440 RH, say, $RH=20\%$, the cloud fraction should exceed 0.8 to prevent total droplet evaporation
 441 in the equilibrium state (at $LWC=1$ g/kg). At the same time, we are interested in the
 442 equilibrium state at which droplets exist. Note that at the lateral edges of warm Cu a shell of
 443 humid air arises around cloud, so RH of the entrained air should be high enough (e.g. Gerber
 444 et al., 2008).

445

446 **Figure 8 here**

447

448 The curve plotted for the time instance of 300 s corresponds to the equilibrium state (hereafter
 449 the equilibrium curve). The curves above the equilibrium curve correspond to the initially
 450 cloudy volume, and the curves below the equilibrium curve correspond to the initially dry
 451 volume. One can see how curves of both types approach the same final state. During the

452 mixing the curves move over the $\left(\frac{r_v}{r_{v0}}\right)^3 - \mu$ plane toward the equilibrium curve. As a result,

453 the curves plotted in Fig.8, corresponding to different time instances of the mixing, together
 454 cover the entire area of the panels.

455 During this movement the distance from the curves to the horizontal line $\left(\frac{r_v}{r_{v0}}\right)^3 = 1$ changes,
 456 and the curves slopes increase. In our case of $L = 40$ m, the mixing remains inhomogeneous
 457 the during entire mixing process, so the change in the distance from the curves to the
 458 horizontal line $\left(\frac{r_v}{r_{v0}}\right)^3 = 1$ characterizes the temporal changes over the mixing process, but not
 459 a change in mixing type.

460 It is noteworthy in this relation that scattering diagrams plotted using *in-situ* observations
 461 reflect mixing between different multiple volumes at different stages of the mixing process.
 462 Accordingly, points in the scattering diagrams can be far from the equilibrium location. Fig. 8
 463 indicates, therefore, that scattering diagrams show snapshots of transient mixing process when
 464 the distance from points in the diagrams to line $\left(\frac{r_v}{r_{v0}}\right)^3 = 1$ characterize the stage of the
 465 mixing process, but not the mixing type.

466 The dependences of normalized cube of the mean volume radius on the cloud fraction at
 467 different time instances at wide DSD also indicate approaching to the equilibrium curve,
 468 while all the curves correspond to $\left(\frac{r_v}{r_{v0}}\right)^3 > 1$ (not shown).

469 Note that in several studies normalized effective radius is used for plotting scattering and
 470 mixing diagrams, but not mean volume radius (Gerber et al. 2008; Freud et al., 2011).
 471 Comparison of scattering and mixing diagrams in the study plotted using mean volume and
 472 effective radii did not reveal any significant differences (not shown).

473

474 **4.2. Mixing diagrams**

475 Using the diffusion-evaporation equations (15-17) we calculated the equilibrium DSD for
 476 different initial relative humidity values and different cloud fractions. Each calculation was

477 performed for both narrow and wide initial DSD (parameters shown in Tab.1). These
 478 equilibrium DSD were used to calculate mixing diagrams showing dependences of normalized
 479 cube of the effective radius on the cloud fraction.

480 The corresponding mixing diagrams for homogeneous mixing case were also calculated
 481 for comparison. To this effect, the supersaturation and DSD in both the cloud and the dry
 482 volumes were aligned, taking into account the cloud fraction value μ . The alignment led to
 483 the following initial values of supersaturation and DSD within the mixing volume:

484

$$485 \quad S_0 = (1 - \mu)S_2; \quad g_0(\sigma) = \mu g_1(\sigma) \quad (21)$$

486

487 Upon the alignment, time evolution values of DSD under homogeneous evaporation in an
 488 adiabatic immovable parcel were calculated until the equilibrium state was reached. These
 489 equilibrium DSD were used to calculate mixing diagrams for homogeneous mixing. To do
 490 this, we used the parcel model proposed by Korolev (1995) that describes evaporation by
 491 means of equations with temperature-dependent parameters. **Figure 9** shows the mixing
 492 diagrams plotted for initial narrow and wide DSD cases.

493

494 **Figure 9 here**

495

496

497 While all the curves in the mixing diagram for narrow DSD are below the straight line

498 $\left(\frac{r_v}{r_{v0}}\right)^3 = 1$, the curves for wide DSD are above this line. The explanation of this effect is given

499 in Section 3 (Fig. 6). The curves plotted for homogeneous and inhomogeneous mixing

500 demonstrate an important feature. Namely, at given values of RH and q_{w1} in the initially dry

501 volume, the values μ_{cr} of the cloud fraction at which all the droplets evaporate are

502 approximately the same for any type of mixing. This condition is the consequence of the mass
 503 conservation law determined by Eq. (11) and does not depend of the initial DSD shape. In
 504 standard mixing diagrams (e.g. Lehmann et al., 2009; Gerber et al., 2008; Freud et al., 2011),
 505 the horizontal straight line $\left(\frac{r_v}{r_{v0}}\right)^3 = 1$ (or $\left(\frac{r_e}{r_{e0}}\right)^3 = 1$) is typically plotted for the entire range of
 506 the cloud fraction [0...1], while the curves corresponding to homogeneous mixing are plotted
 507 for different RH within the range $[\mu_{cr}(RH_2)...1]$. As a result, the high difference between
 508 extremely inhomogeneous and homogeneous mixing types is clearly seen at low RH and at
 509 small cloud fractions. The condition that μ_{cr} is the same for different mixing types indicates
 510 that the mixing diagrams may look nearly similar for $\mu > \mu_{cr}$. It means that the range of the
 511 cloud fractions required for comparison of diagrams aimed at determination of a mixing type
 512 shortens as RH_2 values in the surrounding air decrease.

513 The comparison of the left and the right panels in Fig. 9 shows that the differences
 514 between the diagrams for homogeneous and inhomogeneous mixing types are more
 515 pronounced for initially narrow DSD. The maximum difference should take place for
 516 monodisperse DSD considered in in Pt1, Pt2 and Pt3. Within the range of $\mu > \mu_{cr}$, the
 517 distance between the curves corresponding to different mixing regimes is small even for
 518 narrow DSD and low RH_2 . The lower difference is related to the fact that at high RH_2 the
 519 curves in the mixing diagrams are close to the horizontal straight line in both regimes, while at
 520 low RH_2 , μ_{cr} is small and both curves should drop to zero in the vicinity of $\mu = \mu_{cr}$.

521 As regards the wide DSD case, the difference between the curves corresponding to
 522 different mixing type is negligible (Fig. 9, right)

523

524 **4.3. Effect of the relative humidity**

525 In measurements carried out at cloud boundaries and in cloud simulations, the cloud
 526 fraction is not known, therefore it is widely accepted to use normalized droplet concentration
 527 instead of the cloud fraction (Burnet and Brenguier, 2007; Gerber et al., 2008; Lehmann et al.,
 528 2009). Droplet concentration is normalized by the maximum value along the airplane traverse.
 529 The difference between the cloud fraction and normalized droplet concentration is obvious:
 530 the cloud fraction is a parameter given as the initial condition. At the same time, normalized
 531 droplet concentration changes with time and space due to complete evaporation of some
 532 droplet fraction. **Figure 10** shows dependencies of normalized droplet concentration on the
 533 cloud fraction at the equilibrium final state of mixing. One can see a substantial deviation
 534 from 1:1 linear dependence, especially at low RH. As we know, droplet concentration
 535 decreases in the course of both homogeneous and inhomogeneous mixing if the initial DSD
 536 are polydisperse. The fraction of totally evaporating droplets increases with decreasing RH_2 .
 537 As expected, droplet concentration in homogeneous mixing is higher than that in
 538 inhomogeneous mixing. The difference between droplet concentrations at wide DSD is lower
 539 than at narrow DSD.

540

541 **Fig. 10 here**

542

543 **Figure 11** shows the dependencies $\left(\frac{r_v}{r_{v0}}\right)^3$ on normalized droplet concentration for narrow
 544 and wide DSD in inhomogeneous mixing. The normalization by droplet concentration in the
 545 initially cloud volume at $t=0$ was used. Taking into account the dependences of normalized
 546 droplet concentration on the cloud fraction μ (Fig. 10), one can get the curves shown in Fig.
 547 11 which actually coincide at different RH_2 . The lack of the sensitivity to RH_2 can be
 548 attributed to the fact that a decrease in RH leads to a decrease in normalized droplet
 549 concentration, so the curves corresponding to low RH in Fig. 9 shift to the left when the

550 normalized droplet concentration is used instead of μ . The shape of the dependences in Fig
 551 11 (right) is explained by an increase in the mean volume radius with decreasing droplet
 552 concentration.

553

554 **Fig 11 here**

555

556 Thus, the mixing diagrams plotted in the plane $\left(\frac{r_v}{r_{v0}}\right)^3$ vs normalized droplet
 557 concentration do not depend on the relative humidity of the surrounding dry air. This result
 558 indicates an additional difficulty in distinguishing between mixing types based on scattering
 559 diagrams plotted using *in-situ* data in these axes. The concentration of observed points in
 560 these scattering diagrams close to the line $\left(\frac{r_v}{r_{v0}}\right)^3 = 1$ is often interpreted as an indication of
 561 homogeneous mixing, but at high RH in the surrounding air (Gerber et al., 2008; Lehmann et
 562 al., 2009). High values of RH in the penetrating air volumes are usually explained by
 563 formation of a layer of moist air around the cloud boundary (Gerber et al., 2008, Knight and
 564 Miller, 1998).

565 The reference values of droplet concentration and the effective radius used for
 566 normalization in the present study are taken as the initial values in the cloud volume before it
 567 mixes with the neighbouring dry volume. In real *in-situ* measurements the reference values of
 568 these quantities are typically chosen in a less diluted cloud volume along the airplane traverse.
 569 This reference volume may be quite remote from the particular mixing volume. It can lead to
 570 a shift of the mixing diagram with respect to the $\left(\frac{r_v}{r_{v0}}\right)^3 = 1$ line, as well as to a large variation
 571 in mixing diagram shapes, unrelated, however, to the mixing type (e.g., Lehmann et al.,
 572 2009).

573

574 **5. Discussion and conclusion**

575 This study extends the analysis of mixing performed in Pt3 where the diffusion-
576 evaporation equation served as the basis, the initial DSD were assumed monodisperse and
577 the cloud fraction was chosen as $\mu = 1/2$. In the present study, the analysis focuses on the
578 temporal and spatial evolution of initially polydisperse DSD and investigates mixing diagrams
579 obtained for narrow and wide initial DSD within a wide range of the cloud fraction values (0.1
580 - 0.95). It is shown that results of mixing and the structure of mixing diagrams depend on the
581 initial DSD shape. This finding indicates that mixing is a multi-parametrical problem that
582 cannot be determined by a single parameter (e.g. the Damköhler number as often assumed) or
583 even by two parameters (the Damköhler number and the potential evaporation parameters as
584 assumed in Pt3). The temporal changes of DSD and their moments during mixing are
585 calculated. Although DSD broaden, they tend to remain similar to the original DSD. The main
586 changes come from the cloud air dilution by the dry air, which leads to a decrease in droplet
587 concentration for all droplet sizes. The changes of DSD and its shape are minimum in the
588 initially cloud volumes, especially at significant cloud fractions. The droplet radii
589 corresponding to the DSD peak do not change anyhow significantly. In the initially dry
590 volumes, mixing and evaporation of penetrated droplets leads to a rapid increase in RH.
591 Consequently, large droplets penetrating these volumes do not change their sizes significantly.
592 As a result, the mean volume radius in these volumes rapidly increases and reaches the values
593 typical of cloud volumes, while LWC remains lower than in the cloud volume for most of the
594 mixing time. At narrow DSD, the mean volume (and effective) radius remains smaller than
595 that in the initially cloud volume. At wide DSD, the mean volume (and effective) radius may
596 become larger than that in the initial DSD. This increase in the effective radius is attributed to
597 the fact that evaporation of smaller droplets leads to the increase in the fraction of larger
598 droplets in the DSD. In this study, and in Pt3 it is shown that mixing leads to DSD

599 broadening. This contrasts with the classical theory, when initially monodisperse DSDs
 600 remain monodisperse in course of mixing. This problem is analyzed in detail in Pt 3. Note
 601 that in real clouds DSD there are many mechanism leading to DSDs broadening (e.g. Pinsky
 602 and Khain 2002).

603 Dependences of normalized cube of the mean volume radius on the cloud fraction
 604 $(r_v / r_{v0})^3$ as a function of μ at different time instances form the set of curves filling the entire
 605 $(r_v / r_{v0})^3 - \mu$ plane. Therefore, both the slope and the distance of these curves in respect to
 606 the horizontal line $(r_v / r_{v0})^3 = 1$ change with time. It means that this distance characterizes
 607 the temporal changes in the course of mixing, but not the mixing type (which remains
 608 inhomogeneous during the entire mixing time). The mixing process is comparatively long
 609 (several minutes), so the final equilibrium stage is hardly achievable in real clouds.

610 It is highly significant that the critical values of the cloud fraction μ_{cr} corresponding to
 611 total droplet evaporation are the same for any mixing type. It means that the curves in a
 612 mixing diagram corresponding to homogeneous and inhomogeneous mixing types should be
 613 compared only within the range of $\mu > \mu_{cr}$. The range width of $\mu > \mu_{cr}$ decreases with
 614 decreasing relative humidity in the initially dry volume. Taking into account significant
 615 scattering of observed points, this condition greatly hampers the problem of how to
 616 distinguish between mixing types,

617 Another important result of the study is that mixing diagrams for homogeneous and
 618 inhomogeneous mixing plotted for polydisperse DSD do not differ much. The largest
 619 difference takes place for initially narrow DSD (the maximum difference takes place for
 620 initially monodisperse DSD), but even in this case the difference is not large enough to
 621 reliably distinguish mixing type, owing the significant scatter of observed data. At wide DSD,
 622 this difference between mixing diagrams for homogeneous and inhomogeneous becomes
 623 negligibly small.

624 The cloud fraction μ is a predefined parameter and is not determined from observations.
625 Consequently, in the analysis of *in-situ* measurements the normalized droplet concentration is
626 typically used instead of the cloud fraction. However, there is a significant difference
627 between the cloud fraction prescribed a priori and the normalized droplet concentration that
628 changes due to total evaporation of some fraction of droplets. We have shown that the
629 utilization of normalized droplet concentration in mixing diagrams is not equivalent to the
630 utilization of the cloud fraction. The important conclusion is that when mixing diagrams are
631 plotted using the normalized concentration, the sensitivity to RH disappears. This conclusion
632 is valid even when RH in the initially dry volume is as low as 60%. This conclusion clearly
633 contradicts the wide-spread assumption that mixing types can be easily distinguished in
634 mixing diagrams in case of low relative humidity of the surrounding air.

635 In the present study as well as in Pt3 and LES performed by Andrejczuk et al. (2006, 2009),
636 Khain et al. (2017) it is shown that time needed to establishing of equilibrium either quite long or
637 even never reached. It means that the scattering diagrams observed in situ are just snapshots of
638 the transient mixing process. However, since the classic mixing diagrams are plotted namely for
639 equilibrium states, we investigate the transition to such equilibrium assuming that the mixing
640 volume remains adiabatic (i.e. isolated) during the entire period of mixing. This is, of course, a
641 serious simplification made to compare the results with those predicted by classical concept.

642 To sum up, our general conclusion is that the simplifications underlying the classical
643 concept of mixing are too crude, making it impossible to use mixing diagrams for
644 comprehensive analysis of mixing and especially for determination of mixing types. At the
645 same time, mixing diagrams may contain useful information concerning the DSD width.

646

647 ***Acknowledgements***

648 This research was supported by the Israel Science Foundation (grants 1393/14, 2027/17)
 649 and the Office of Science (BER) of the US Department of Energy (Award DE-SC0006788,
 650 DE-FOA-0001638). Codes of the diffusional-evaporation model are available upon request.

651 .

652

653

654

655 **Appendix. List of symbols**

Symbol	Description	Units
A_2	$\frac{1}{q_v} + \frac{L_w^2}{c_p R_v T^2}$, coefficient	-
a_n	Fourier series coefficients	-
C	Richardson's law constant	-
c_p	specific heat capacity of moist air at constant pressure	$\text{J kg}^{-1}\text{K}^{-1}$
D	coefficient of water vapor diffusion in air	$\text{m}^2 \text{s}^{-1}$
Da	<i>Damköhler</i> number	-
e	water vapor pressure	N m^{-2}
e_w	saturation vapor pressure above flat surface of water	N m^{-2}
F	$\left(\frac{\rho_w L_w^2}{k_a R_v T^2} + \frac{\rho_w R_v T}{e_w(T) D} \right)$, coefficient	$\text{m}^{-2} \text{s}$
$f(r)$	droplet size distribution	m^{-4}
$g(r)$	droplet size distribution	m^{-5}
$g_0(\sigma)$	initial distribution of square radius in homogeneous mixing	m^{-5}
$g_1(\sigma)$	initial distribution of square radius	m^{-5}
k_a	coefficient of air heat conductivity	$\text{J m}^{-1}\text{s}^{-1}\text{K}^{-1}$

K	turbulent diffusion coefficient	m^2s^{-1}
L	characteristic spatial scale of mixing	m
L_w	latent heat for liquid water	J kg^{-1}
N	droplet concentration	m^{-3}
N_0	Parameter of Gamma distribution	m^{-3}
\bar{N}	mean droplet concentration	m^{-3}
N_1	initial droplet concentration in cloud volume	m^{-3}
P	pressure of moist air	N m^{-2}
q_v	water vapor mixing ratio (mass of water vapor per 1 kg of dry air)	-
q_w	liquid water mixing ratio (mass of liquid water per 1 kg of dry air)	-
q_{w1}	liquid water mixing ratio in cloud volume	-
R	$\frac{S_2}{A_2 q_{w1}}$, non-dimensional parameter	-
R_a	specific gas constant of moist air	$\text{J kg}^{-1}\text{K}^{-1}$
R_v	specific gas constant of water vapor	$\text{J kg}^{-1}\text{K}^{-1}$
r	droplet radius	m
r_1	initial droplet radius	m
r_e	effective radius	m
r_{e0}	initial effective radius	m
S	$e/e_w - 1$, supersaturation over water	-
S_2	initial supersaturation in the dry volume	-
S_0	initial supersaturation in homogeneous mixing	-

T	temperature	K
t	time	s
x	distance	m
α	parameter of Gamma distribution	-
β	parameter of Gamma distribution	m^{-1}
Δt	time step	s
μ	cloud fraction	-
μ_{cr}	critical cloud fraction	-
ε	turbulent dissipation rate	m^2s^{-3}
$\Gamma(x,t)$	conservative function	-
ρ_a	air density	kg m^{-3}
ρ_w	liquid water density	kg m^{-3}
σ	square of droplet radius	m^2

656

657

658

659

660

661

662

663

664

665

666

667

668

669

670

671

672 **References**

673

674 Andrejczuk, M., W. W. Grabowski, S. P. Malinowski, and P. K. Smolarkiewicz, 2006:
675 Numerical simulation of cloud– clear air interfacial mixing: Effects on cloud microphysics. *J.*
676 *Atmos. Sci.*, **63**, 3204–3225.

677 Andrejczuk, M., W. W. Grabowski, S. P. Malinowski, and P. K. Smolarkiewicz, 2009:
678 Numerical simulation of cloud–clear air interfacial mixing: Homogeneous versus
679 inhomogeneous mixing, *J. Atmos. Sci.*, **66(8)**, 2493-2500, doi:10.1175/2009JAS2956.

680 Bera, S., T. V. Prabha, and W. W. Grabowski, 2016a: Observations of monsoon
681 convective cloud microphysics over India and role of entrainment-mixing, *J. Geophys. Res.*
682 *Atmos.*, **121**, 9767–9788, doi:10.1002/2016JD025133.

683 Bera, S., G. Pandithurai and T. V. Prabha, 2016b: Entrainment and droplet spectral
684 characteristics in convective clouds during transition to monsoon. *Atmos. Sci. Lett.* **17**, 286–
685 293.

686 Boffetta, G. and Sokolov, I. M., 2002: Relative dispersion in fully developed turbulence:
687 The Richardson’s law and intermittency correction, *Phys. Rev. Lett.*, **88**, 094501,
688 doi:10.1103/PhysRevLett.88.094501.

689 Burnet, F., and J.-L. Brenguier, 2007: Observational study of the entrainment-mixing
690 process in warm convective cloud, *J. Atmos. Sci.*, **64**, 1995–2011.

691 Devenish B. J., P. Bartello, J.-L. Brenguier, L.R. Collins, W.W. Grabowski, R.H.A.
692 Ijzermans, S.P. Malinowski, M.W. Reeks, J.C. Vassilicos, L-P. Wang, and Z. Warhaft, 2012:
693 Droplet growth in warm turbulent clouds. *Q. J. Roy. Meteorol. Soc.*, **138**, 1401-1429.

- 694 Freud, E., D. Rosenfeld, and J. R. Kulkarni, 2011: Resolving both entrainment mixing and
695 number of activated CCN in deep convective clouds, *Atmos. Chem. Phys.*, **11**, 12,887–12,900,
696 doi:10.5194/acp-11-12887-2011.
- 697 Gerber H, Frick G, Jensen J.B, and Hudson J.G., 2008: Entrainment, mixing, and
698 microphysics in trade-wind cumulus. *J. Meteorol. Soc. Jpn.*, **86A**. 87-106.
- 699 Khain, A. P., M. Ovchinnikov, M. Pinsky, A. Pokrovsky, and H. Krugliak, 2000: Notes on
700 the state-of-the-art numerical modeling of cloud microphysics. *Atmos. Res.*, **55**, 159-224.
- 701 Khain A., Thara V. Prabha, N. Benmoshe, G. Pandithurai, M. Ovchinnikov, 2013: The
702 mechanism of first raindrops formation in deep convective clouds. *J. Geoph. Res.*
703 *Atmospheres*, **118**, 9123–9140.
- 704 Khain A., M. Pinsky and L. Magaritz-Ronen, 2017: Physical interpretation of mixing
705 diagrams. *J. Geophys. Res.* (in revision)
- 706 Knight C. A. and L. J. Miller, 1998: Early radar echoes from small, warm cumulus: Bragg
707 and hydrometeor scattering. *J. Atmos. Sci.*, **55**, 2974-2992.
- 708 Korolev, A.V., 1995: The influence of supersaturation fluctuations on droplet size spectra
709 formation. *J. Atmos. Sci.*, **52**, 3620-3634.
- 710 Korolev A., and I. Mazin, 2003: Supersaturation of water vapor in clouds, *J. Atmos. Sci.*,
711 **60**, 2957-2974.
- 712 Korolev, A., Khain, A., Pinsky, M., and French, J., 2016: Theoretical study of mixing in
713 liquid clouds – Part 1: Classical concept, *Atmos. Chem. Phys.*, **16**, 9235–9254.
- 714 Kovetz, A., and B. Olund, 1969: The effect of coalescence and condensation on rain
715 formation in a cloud of finite vertical extent. *J. Atmos. Sci.*, **26**, 1060–1065.
- 716 Krueger, S. K., Lehr, P. J., & Su, C. W., 2006: How entrainment and mixing scenarios
717 affect droplet spectra in cumulus clouds. In *12th Conference on Cloud Physics, and 12th*
718 *Conference on Atmospheric Radiation*, Madison, WI.

- 719 Kumar, B., J. Schumacher, and R. A. Shaw, 2014: Lagrangian mixing dynamics at the
720 cloudy–clear air interface. *J. Atmos. Sci.*, **71**, 2564-2579.
- 721 Kumar, B., S. Bera, T. V. Prabha, and W. W. Grabowski, 2017: Cloud-edge mixing:
722 Direct numerical simulation and observations in Indian Monsoon clouds, *J. Adv. Model. Earth
723 Syst.*, **9**, doi:10.1002/2016MS000731.
- 724 Lehmann, K., H. Siebert, and R. A. Shaw, 2009: Homogeneous and inhomogeneous
725 mixing in cumulus clouds: Dependence on local turbulence structure. *J. Atmos. Sci.*, **66**, 3641-
726 3659.
- 727 Magaritz-Ronen. L., M. Pinsky, and A. Khain, 2016: Drizzle formation in stratocumulus
728 clouds: effects of turbulent mixing. *Atmos. Chem. Phys.*, **16**, 1849–1862, doi:10.5194/acp-16-
729 1849.
- 730 Monin, A.S. and Yaglom, A.M. 1975: “Statistical Fluid Mechanics: Mechanics of
731 Turbulence”, vol. **2**, MIT Press.
- 732 Pinsky, M., Khain, A. P., 2002: Effects of in-cloud nucleation and turbulence on droplet
733 spectrum formation in cumulus clouds. *Quart. J. Roy. Met. Soc.*, **128**, 1-33.
- 734 Pinsky, M., Khain, A., Korolev, A., and Magaritz-Ronen, L., 2016a: Theoretical
735 investigation of mixing in warm clouds – Part 2: Homogeneous mixing, *Atmos. Chem. Phys.*,
736 **16**, 9255–9272.
- 737 Pinsky, M., Khain, A., and Korolev, A., 2016b: Theoretical analysis of mixing in liquid
738 clouds – Part 3: Inhomogeneous mixing, *Atmos. Chem. Phys.*, **16**, 9273–9297.
- 739 Polyanin A. D. and V. F. Zaitsev, 2004: Handbook of nonlinear partial differential
740 equations. Chapman & Hall/CRC, 809 pp.
- 741 Prabha T. , Khain, A. P., B. N. Goswami, G. Pandithurai, R. S. Maheshkumar, and J. R.
742 Kulkarni, 2011: Microphysics of pre-monsoon and monsoon clouds as seen from in-situ
743 measurements during CAIPEEX. *J. Atmos. Sci.*, **68**, 1882-1901.

744 Pruppacher, H.R., Klett, J.D., 1997. *Microphysics of Clouds and Precipitation*. 2nd edn.
745 Oxford Press, 914 p.

746 Segal, Y., Khain, A. P., and M. Pinsky, 2003: Thermodynamic factors influencing the
747 bimodal spectra formation in cumulus clouds. *Atmos. Res.* **66**, 43-64.

748 Yang F., R. Shaw, and H. Xue, 2016: Conditions for super-adiabatic droplet growth
749 after entrainment mixing *Atmos. Chem. Phys.*, **16**, 9421–9433, [www.atmos-chem-](http://www.atmos-chem-phys.net/16/9421/2016/)
750 [phys.net/16/9421/2016/](http://www.atmos-chem-phys.net/16/9421/2016/) doi:10.5194/acp-16-9421-2016.

751 Yum, S. S., J. Wang, Y. Liu, G. Senum, S. Springston, R. McGraw, and J. M. Yeom,
752 2015: Cloud microphysical relationships and their implication on entrainment and mixing
753 mechanism for the stratocumulus clouds measured during the VOCALS project, *J. Geophys.*
754 *Res.*, **120(10)**, 5047-5069, 10.1002/2014JD022802.

755

756

757

758

759

760

761

762

763

764

765

766

767

768

769

770

771

772

773

774

775

776

777

778

779

780

Tab.1 Parameters of the initial Gamma distributions

DSD	N_0 , cm ³	α	β , μm	Modal radius, μm	LWC, g/m ³
Narrow	264.2	101.0	0.1	10.0	1.178
Wide	71.0	4.3	3.1	10.0	1.178

781

782

783

784

785

786

787

788

789

790

791

792

793

794

795

796

797

798

799

800

801

802

803

804

805

806

807

808

809

810

811

812 **Fig.1.** The initial state at $t=0$. The left volume is a saturated cloudy volume; the right

813 volume is an under-saturated dry air volume.

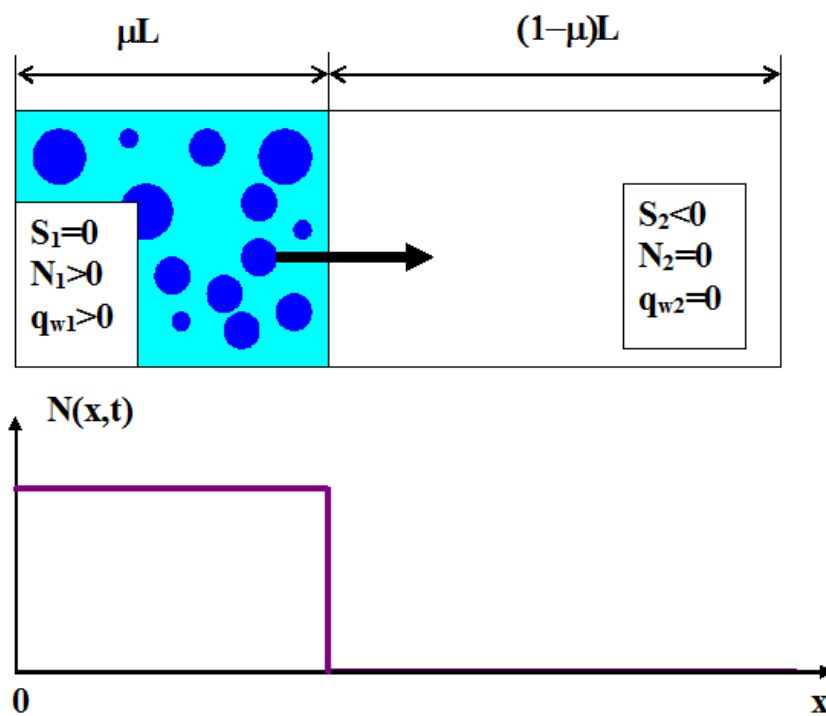
814

815

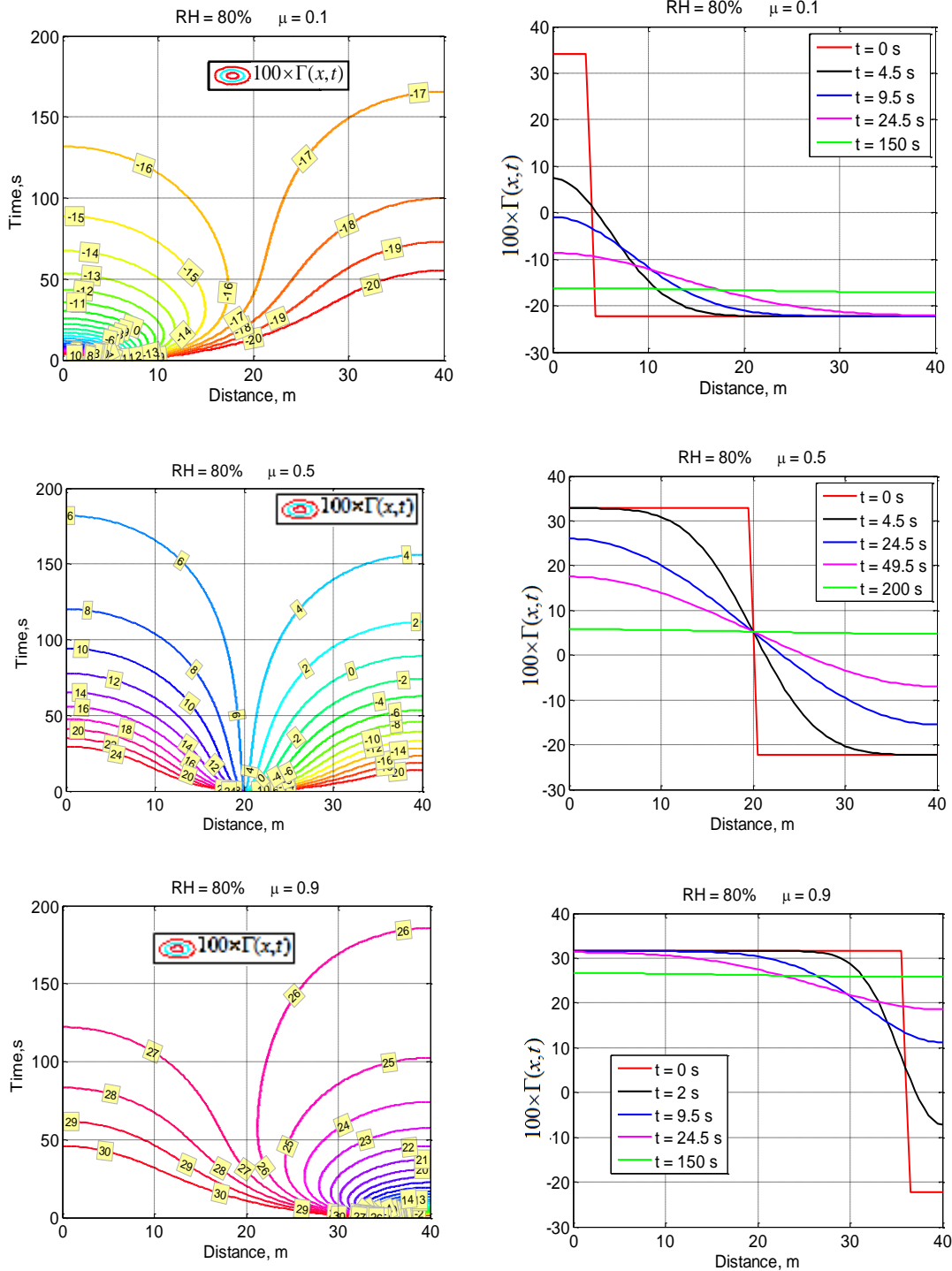
816

817

818



819
 820
 821
 822
 823
 824
 825
 826
 827
 828
 829
 830
 831
 832
 833
 834
 835
 836
 837
 838
 839
 840
 841
 842



843 **Fig. 2.** Spatial-temporal variations of conservative function $100 \times \Gamma(x, t)$ for different cloud
 844 fractions μ and initial $RH_2 = 80\%$.

845

846

847

848

849

850

851

852

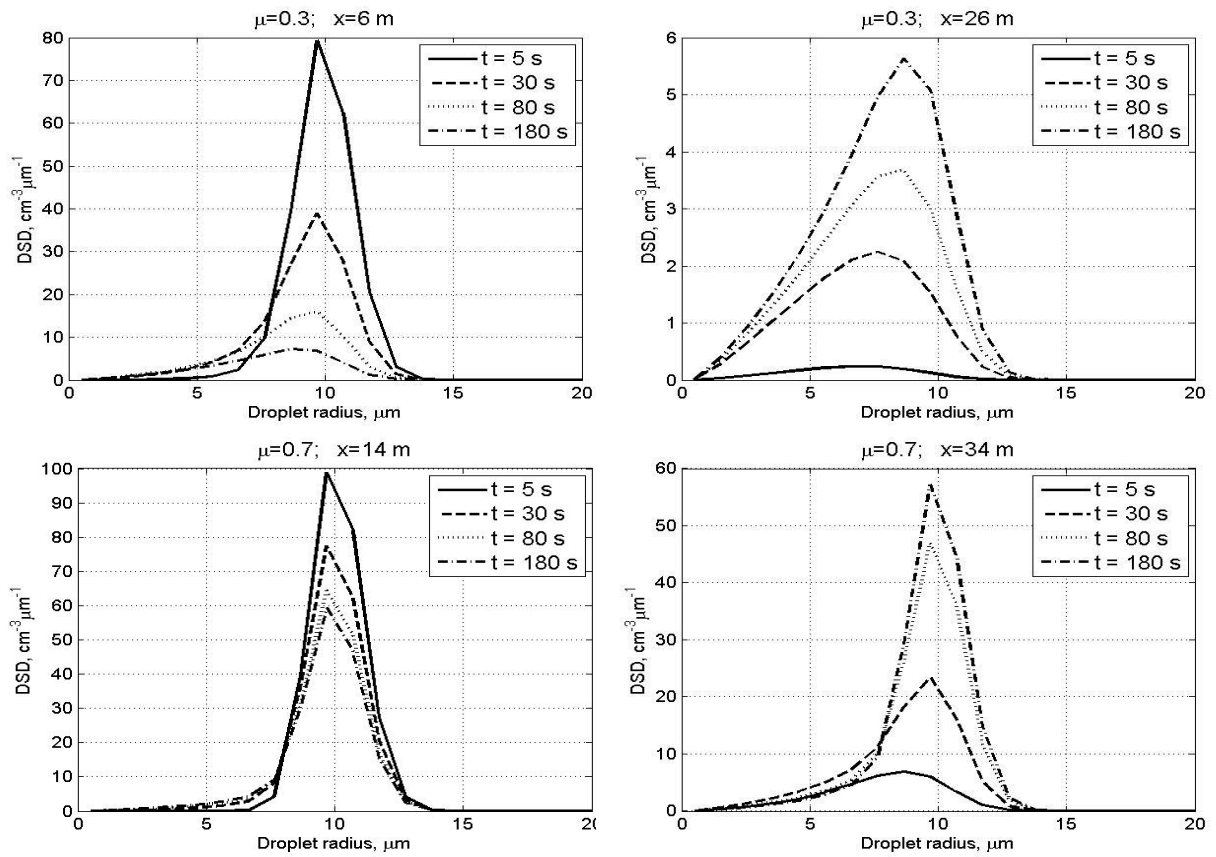
853

854

855

856

857



864

865

866

867

868

869

870

Fig. 3. Time evolution of DSD in the centers of the initially cloudy volume (left) and of the

initially dry air volume (right) at initially narrow DSD. The initial mixing parameters are

$RH_2 = 80\%$, $T = 10^\circ\text{C}$, $p = 828.8$ mb and $L = 40$ m.

871

872

873

874

875

876

877

878

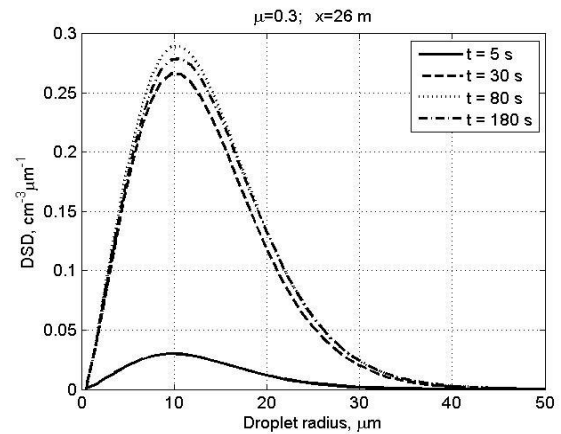
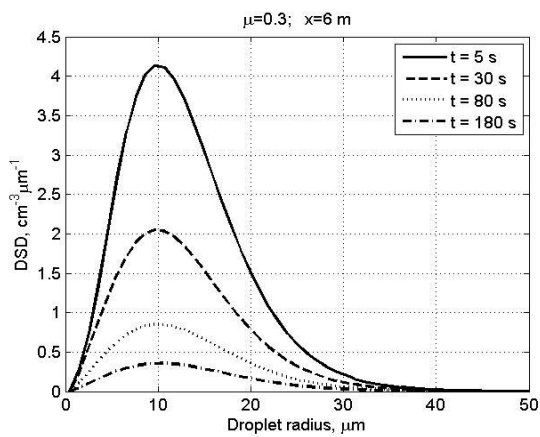
879

880

881

882

883



884

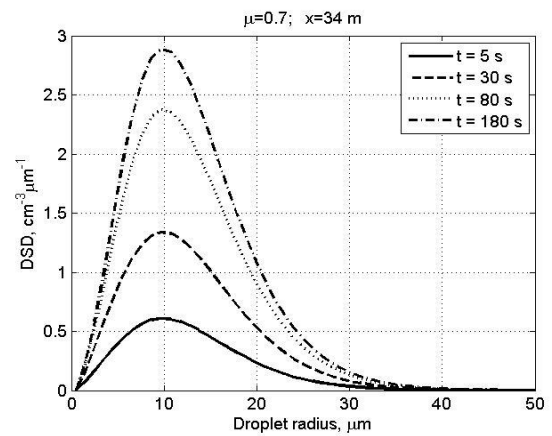
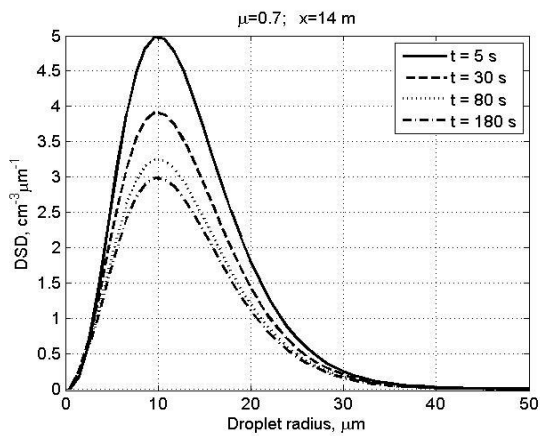
885

886

887

888

889



890

891

892 **Fig. 4.** The same as in Fig. 3, but for the initially wide DSD.

893

894

895

896

897

898

899

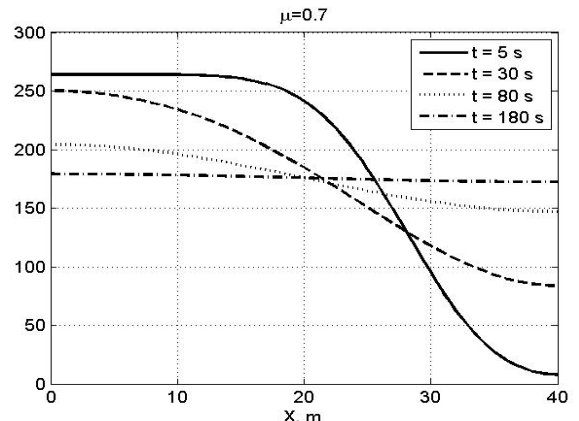
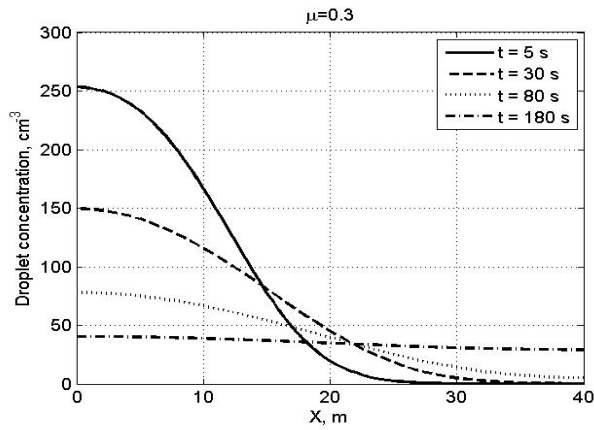
900

901

902

903

904



905

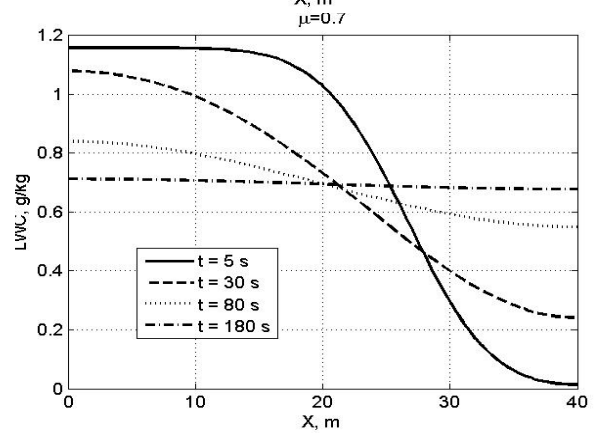
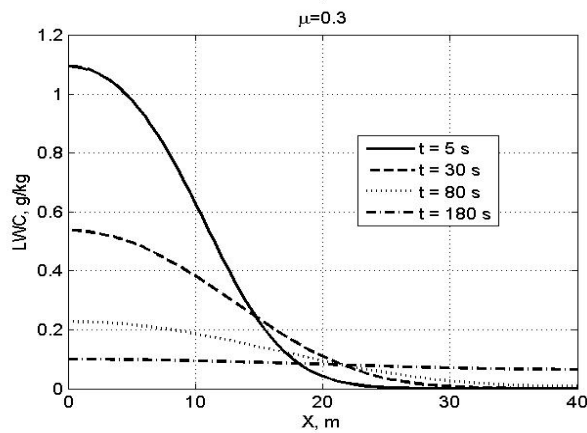
906

907

908

909

910



911

912

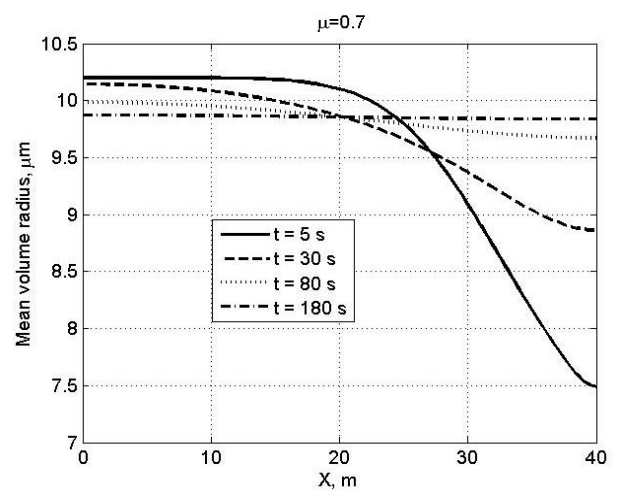
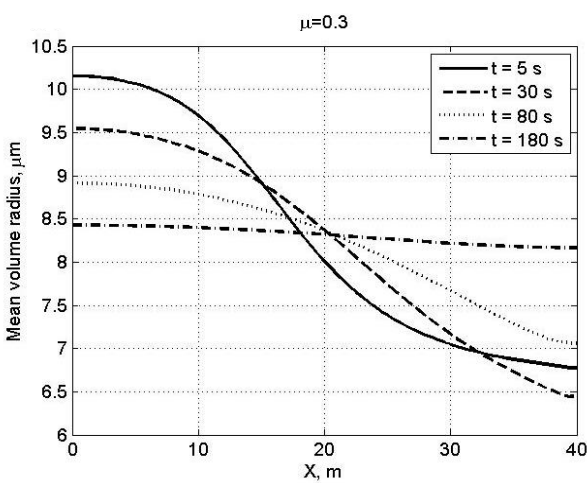
913

914

915

916

917



918

919 **Fig. 5.** Spatial dependences of droplet concentration, LWC and the mean volume radius

920 within the mixing volume at different time instances at narrow initial DSD. The initial mixing

921 parameters are $RH_2 = 80\%$, $T = 10^\circ\text{C}$, $p = 828.8$ mb and $L = 40$ m.

922

923
 924
 925
 926
 927
 928
 929
 930
 931
 932
 933
 934
 935
 936
 937
 938
 939
 940
 941
 942
 943
 944
 945
 946
 947
 948

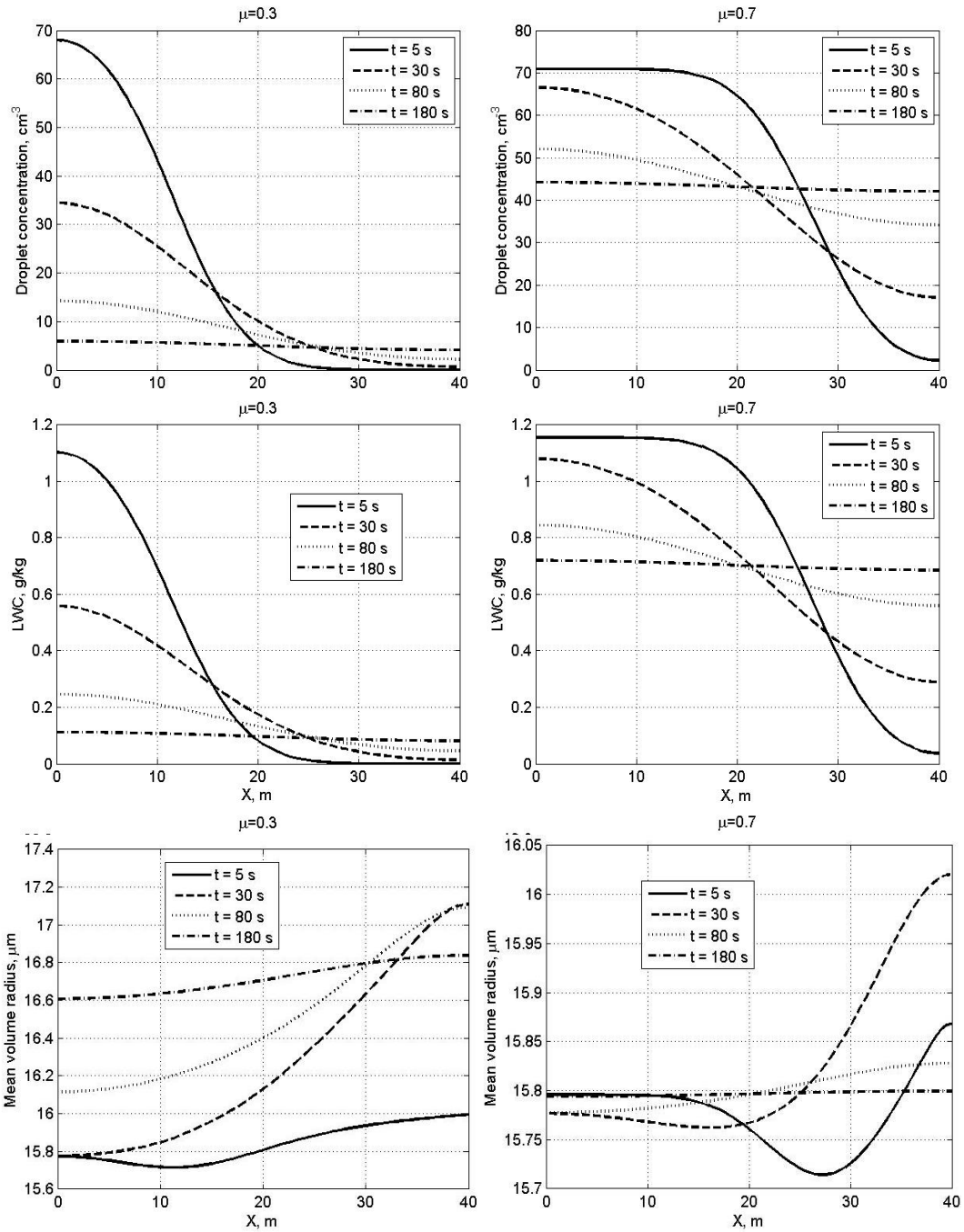


Fig. 6. The same as in Fig. 5, but for wide DSD

949

950

951

952

953

954

955

956

957

958

959

960

961

962

963

964

965

966

967

968

969

970

971

972

973

974

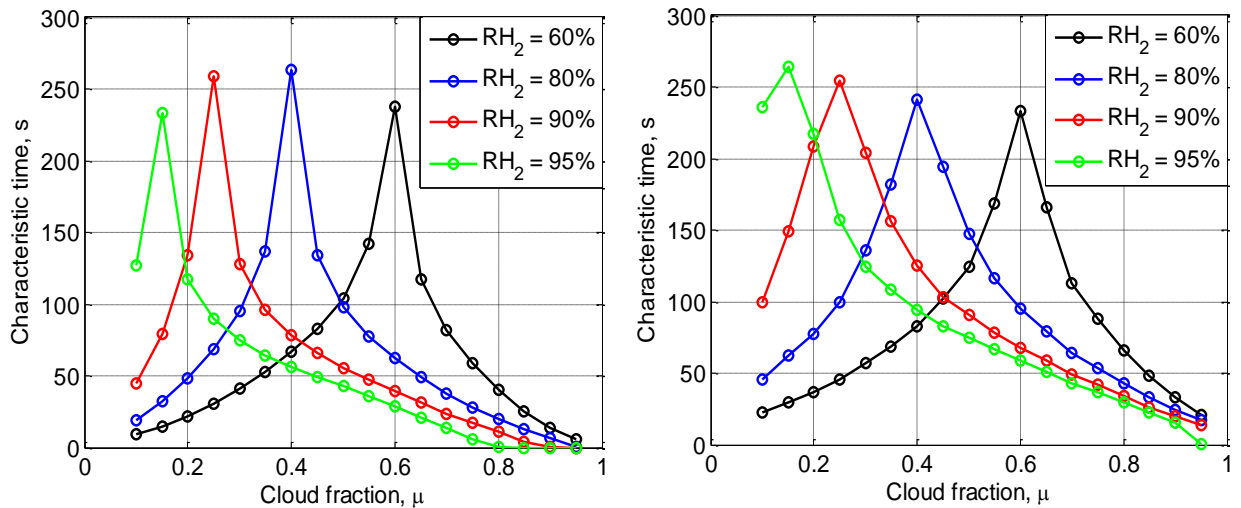


Fig. 7. Time required to reach the equilibrium state vs. the cloud fraction at different initial RH for the initially narrow DSD (left) and the initially wide DSD (right). Parameters of DSD are given in Tab. 1. The initial mixing parameters are $T=10^{\circ}C$, $p=828.8$ mb and $L=40$ m.

975

976

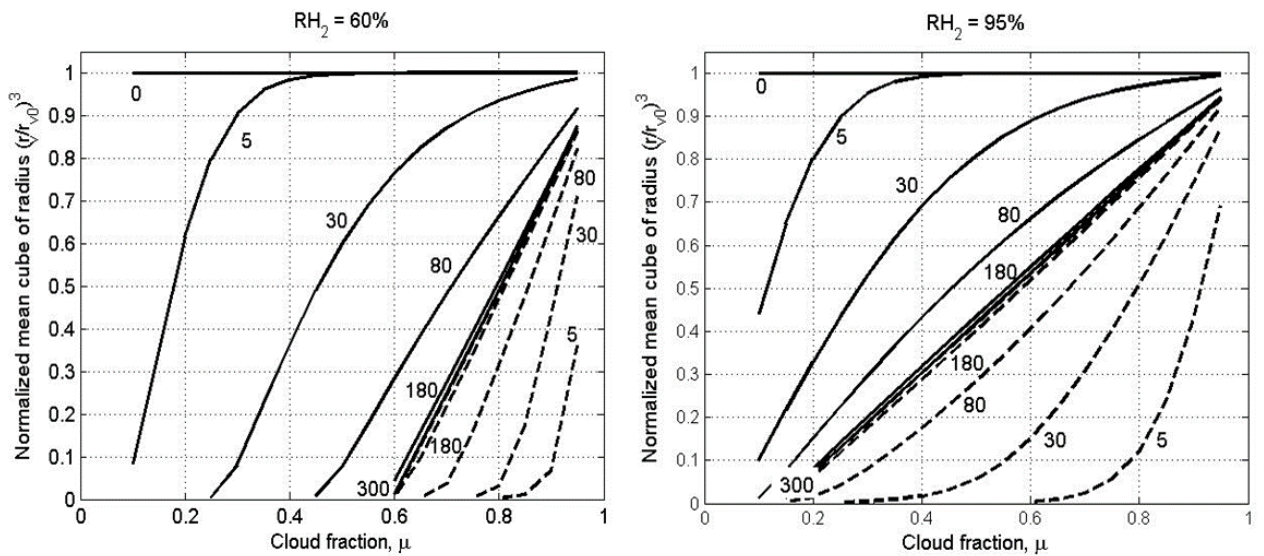
977

978

979

980

981



982

983

984 **Fig. 8.** Dependences of normalized cube of the mean volume radius on the cloud fraction

985 at different time instances for $x=0$ (solid lines) corresponding to the initially cloud volume,

986 and $x=L$ (dash line) corresponding to the initially dry volume. The time instances in seconds

987 are marked by numbers. The figure is plotted for the narrow initial DSD for two values of

988 RH_2 : 60% (left panel) and 95% (right panel). Parameters of DSD are given in Tab. 1. The

989 initial mixing parameters are $T=10^\circ C$, $p=828.8$ mb and $L=40$ m. Calculations performed

990 within the range of $0.1 < \mu < 0.95$.

991

992

993

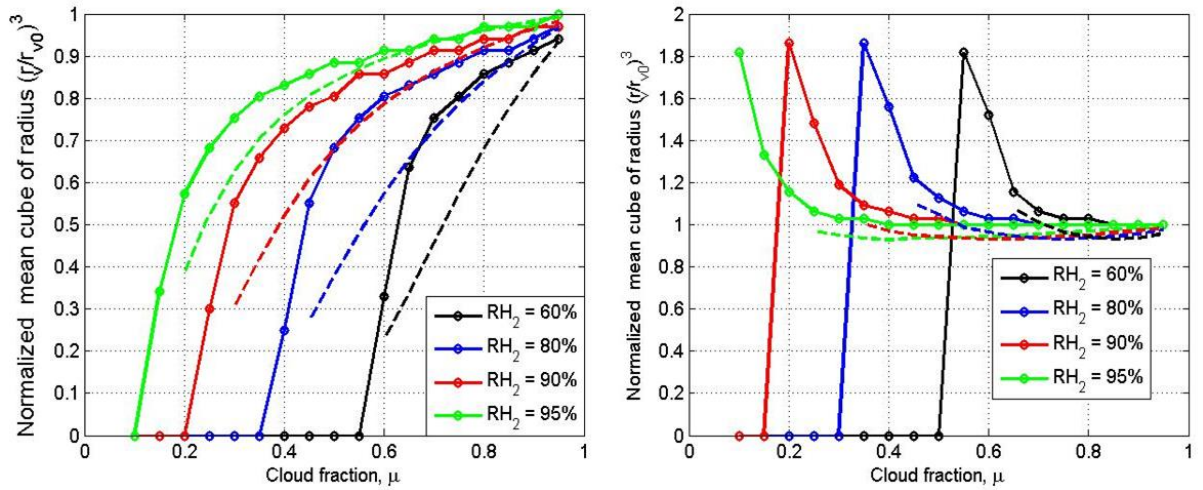
994

995

996

997

998



999

1000

1001

1002 **Fig. 9.** Mixing diagrams. Normalized cube of the mean volume radius vs. the cloud

1003 fraction for initial narrow DSD (left) and initial wide DSD (right). The dependencies

1004 correspond to the equilibrium state. Parameters of initial DSD are presented in Tab. 1. Solid

1005 and dashed lines show the mixing diagrams for inhomogeneous and homogeneous mixing,

1006 respectively. The initial mixing parameters are $T = 10^\circ C$, $p = 828.8$ mb and $L = 40$ m.

1007

1008

1009

1010

1011

1012

1013

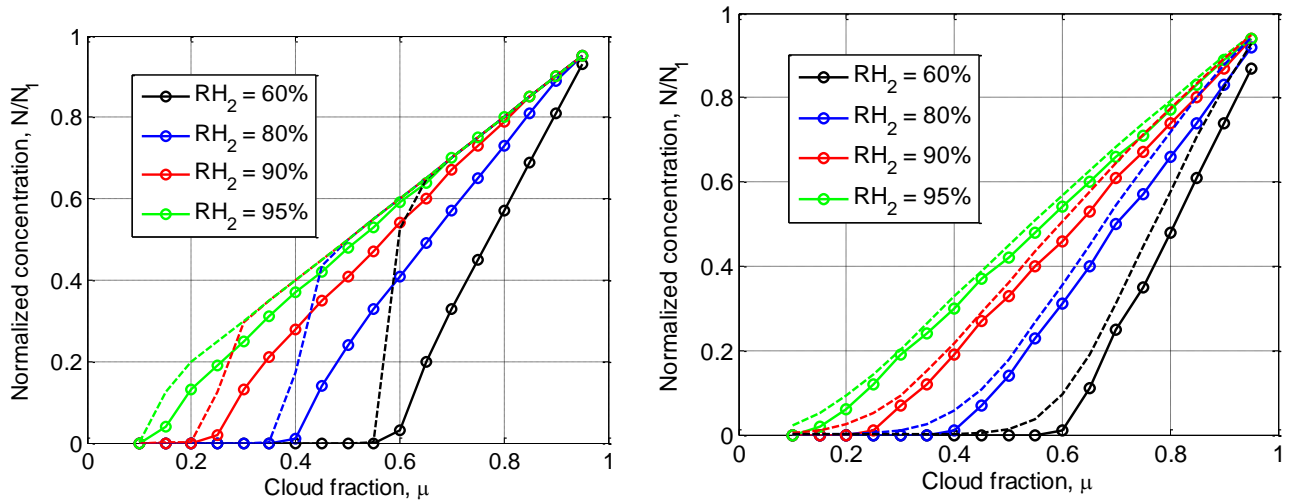


Fig. 10. Final normalized droplet concentration vs. cloud fraction for initially narrow DSD (left) and initially wide DSD (right). Parameters of initial DSD are shown in Tab. 1. Dashed line shows the results of equivalent homogeneous mixing. The initial mixing parameters are $T = 10^\circ C$, $p = 828.8$ mb and $L = 40$ m.

1040

1041

1042

1043

1044

1045

1046

1047

1048

1049

1050

1051

1052

1053

1054

1055 **Fig. 11.** Dependencies of normalized cube of the effective radius on normalized droplet

1056 concentration for different initial relative humidity values. Left panel: narrow initial DSD.

1057 Right panel: wide initial DSD. The initial mixing parameters are $T = 10^\circ\text{C}$, $p = 828.8$ mb

1058 and $L = 40$ m.

1059

1060

1061

